International Journal of Mass Spectrometry 446 (2019) 116232

Contents lists available at ScienceDirect

International Journal of Mass Spectrometry

journal homepage: www.elsevier.com/locate/ijms

Position-dependent microchannel plate gain correction in Rosetta's ROSINA/DFMS mass spectrometer

J. De Keyser [a, b, *], K. Altwegg [c], A. Gibbons [a, d], F. Dhooghe [a], H. Balsiger [c], J.-J. Berthelier [e], S.A. Fuselier [f, g], T.I. Gombosi [h], E. Neefs [i], M. Rubin [c]

[a] Space Physics Division, Royal Belgian Institute for Space Aeronomy, Ringlaan 3, B-1180, Brussels, Belgium
[b] Center for Plasma Astrophysics, Katholieke Universiteit Leuven, Celestijnenlaan 200B, B-3001, Heverlee, Belgium
[c] Physikalisches Institut, University of Bern, Sidlerstr. 5, CH-3012 Bern, Switzerland
[d] Quantum Chemistry and Photophysics Laboratory, Université Libre de Bruxelles, Av. F. D. Roosevelt 50, B-1050, Brussels, Belgium
[e] LATMOS/IPSL-CNRS-UPMC-UVSQ, 4 Av. de Neptune, F-94100, Saint-Maur, France
[f] Space Science Directorate, Southwest Research Institute, 6220 Culebra Road, San Antonio, TX, 78228, USA
[g] Department of Physics and Astronomy, University of Texas at San Antonio, San Antonio, TX, 78249, USA
[h] Department of Atmospheric, Oceanic and Space Sciences, University of Michigan, 2455 Hayward, Ann Arbor, MI, 48109, USA
[i] Engineering Division, Royal Belgian Institute for Space Aeronomy, Ringlaan 3, B-1180, Brussels, Belgium

ARTICLE INFO

Article history:
Received 9 July 2019
Received in revised form
16 September 2019
Accepted 16 September 2019
Available online 19 September 2019

Keywords:
Mass spectrometry
Microchannel plate
Secondary electron yield
Gain correction
Comet atmosphere
Rosetta

ABSTRACT

Mass spectrometers that rely on microchannel plate (MCP) detectors age when they are used intensively. The ageing process is due to a reduction of the MCP gain as ions repeatedly bombard the MCP, leading to a reduction of the secondary electron yield of an impacting ion and to a reduction of the electron amplification within the MCP pores. MCP gain therefore is both time- and position-dependent. This is particularly true for the Double Focusing Mass Spectrometer DFMS, part of the ROSINA instrument, embarked on the European Space Agency's Rosetta spacecraft that studied comet 67P/Churyumov-Gerasimenko continuously for over more than 2 years. A position-dependent gain correction technique is developed here. A detailed assessment of the technique demonstrates that improper treatment of this position-dependent gain can lead to misleading results and false conclusions, especially regarding less abundant species whose mass peak signature overlaps with peaks of abundant species. The correction technique presented here avoids such problems, especially in the situation where detector ageing is significant and uneven across the detector. It is also able to explain why all recorded mass peaks have a nearly symmetric double Gaussian shape, despite the strong variations in the position-dependent gain.

1. Introduction

Mass spectrometers for the analysis of neutral gases consist of an ionization chamber, a mass analyser and a detector [1]. Incoming neutral atoms or molecules are ionized in the ionization chamber, accompanied by some fragmentation into neutral and ionized fragments. The ions are sorted according to their mass-over-charge ratio in the mass analyser. The flux of ions as a function of mass-over-charge is recorded by the detector. Knowledge of the neutral ionization cross sections, the fragmentation patterns, and the detector properties are essential to interpret the observed parent and fragment ion fluxes in terms of the ambient neutral gas density. The present paper deals with mass spectrometry in space, which follows basically the same setup, but which leads to some practical difficulties.

Various types of detectors are used in mass spectrometry [1–3]. The focus here is on microchannel plate (MCP) detectors. MCPs consist of arrays of small pores, often in lead silicate glass, each of which acts as an electron multiplier [4,5]. An incident ion creates secondary electrons, which are accelerated by an electric field along the pore channel that is imposed by a potential difference between the MCP front and back surfaces. These electrons repeatedly hit the channel walls and create even more electrons in an avalanche process. Each pore thus serves as a continuous dynode that can lead to a gain of many orders of magnitude. MCP performance depends on the pore length-to-diameter ratio. Curved or chevron-type

* Corresponding author., Space Physics Division, Royal Belgian Institute for Space Aeronomy, Ringlaan 3, B-1180, Brussels, Belgium.
E-mail address: Johan.DeKeyser@aeronomie.be (J. De Keyser).

https://doi.org/10.1016/j.ijms.2019.116232

dynode channels are preferred in order to minimize ion feedback due to ionization of ambient gas molecules inside the pores and subsequent ion acceleration toward the pore entrance; secondary electron generation by such ions is suppressed by avoiding straight pore channels. The output of the MCP can best be measured by collecting the electrons over a certain time on anode capacitors and by using a Coulombmeter to convert the accumulated charge during this interval into a current. There exist very compact MCP – Coulombmeter combinations, which make them particularly attractive for use in space [2,6].

The MCP pores are typically arranged in a 2D hexagonal pattern [4,5]. Usually only 1D spatial information (mass-over-charge) is needed in mass spectrometers based on magnetic and electric sector mass analysers. In such spectrometers the MCPs provide analogue multiplication of the incoming ion current. The precise MCP gain must be known for interpreting the measured electron current as function of 1D position (discretized in pixels) in terms of the incident ion current (or ion count rate). Time-of-flight mass spectrometers, by contrast, exploit the capability of MCPs to produce short electron pulses for each incident ion [e.g. 1]. The MCP is then used in pulse-counting mode; the gain only serves to enhance pulse height so as to make pulses clearly detectable above the noise level.

The gain changes with time as the MCP ages. Whether MCP ageing is an important issue depends on the incident particles, the detection mode, and the application. If the incident particles are low-energy photons or electrons, the excitation of the pore wall material at the pore entrance is reversible and there is little ageing; there can be minor gain variations that have to do with temperature fluctuations or with electronic stability [7]. If the particles impinging on the MCP are ions or high-energy photons or electrons, on the contrary, the damage sustained at the entrance of the pore can be substantial. The momentum of incident ions may displace atoms in the pore wall material, leading to sputtering and ion implantation [8,9], so that the secondary electron yield is reduced. In all these cases, the inner surface all along the pore channels is bombarded by secondary electrons (especially near the MCP back surface) which also may provoke changes in the material. However, the extent to which this occurs depends on the gain potentials that are used, and these have to do with the detection mode. In pulse-counting mode (or digital mode), the MCP is operated in saturation, i.e. a high post-acceleration potential is used to ensure that each incident particle produces an electron cascade. This leads to more rapid ageing. On one hand, the precise value of the gain does not matter for time-of-flight analysis as long as a pulse is generated with a sufficient amplitude (the saturation value). On the other hand, such ageing will degrade the maximum event detection rate [10]. Problems may also arise when the detector is not operated in saturation to avoid problems with the detection rate and with ion feedback [11]. When using an MCP in analogue mode, however, one must know the gain accurately since it directly relates the detected electron current to the incident particle rate. If no (significant) post-acceleration is used, the total gain depends on the secondary electron yield of the impacting particle, which is a function of incident particle energy and chemical identity [12,13]. The advantage of the analogue approach is the very high dynamic range that can be achieved, especially when adapting the gain potential to the signal strength. Finally also the application is important. In an optical detector imaging star fields, there is only a limited number of detector pixels that receives light and the location of the illuminated spots changes from observation to observation, so that the degradation is averaged out over the detector. In a high-resolution mass spectrometer the mass peaks are always focused more or less onto the centre of the detector, so that pronounced ageing is observed there. The gain reduction is therefore not uniform but depends on the positions and intensities of the mass peaks that have been measured previously, as well as on the ion acceleration energies used in the instrument for these masses.

Determining the position- and time-dependent gain, and exploiting that information to interpret the mass spectra, is not an easy task, and is always specific to the particular mass spectrometer and detector setup. This is especially true for space-borne mass spectrometers, which are subject to additional constraints and are inaccessible once they have been launched, as is the case for the Double Focusing Mass Spectrometer (DFMS), part of the ROSINA instrument on board the Rosetta spacecraft that studied comet 67P/Churyumov-Gerasimenko [14]. The characteristics of the DFMS detector are presented in section 2. Section 3 introduces an improved technique for using the position-dependent gain information in order to obtain properly calibrated mass spectra. This technique relies heavily on the pre-launch characterisation of the MCP-based detector used in DFMS by Ref. [2]. The technique is then applied to synthetic and DFMS data to evaluate its merits (sections 4 and 5). The paper concludes with a summary.

2. The DFMS MCP-LEDA detector

To set the context, this section briefly reviews the DFMS MCP-LEDA detector combination. The description focuses on the essentials needed to understand the position-dependent gain correction.

The DFMS mass spectrometer uses a combination of an electrostatic and a magnetic sector to sort the ions that are produced from the incoming neutral atoms or molecules by electron impact ionization in the ion source (note that the discussion is limited here to the instrument's neutral mode). An entrance slit selection system together with an electrostatic zoom lens allow to switch between a low and a high mass resolution mode [14]; electrostatic deflectors bend the beam as desired to guide it through either the low or the high resolution slit, the former being 6.5× larger than the latter. The high resolution (HR) mode provides $m/\Delta m \approx 3000$ at the 1% level, about 6.4× better than in low resolution (LR) mode. The HR mass window that can be studied in a single measurement is reduced by the same factor relative to the LR case; the instrument is programmed to scan over successive masses to cover a broader mass range.

Ions corresponding to a given species with mass-over-charge ratio m^* arrive at the detector in the form of a focused sheet-like beam (see Fig. 1), which is the image of the entrance slit and has a finite thickness in the mass analysis direction but is extended in the perpendicular direction. The ion intensity across the beam can be described by a single-peaked function $\hat{f}(p)$. As illustrated in Fig. 1 these ions hit the MCP. The ion beam width typically is larger than the dimensions of an MCP pore (6 μm). Note that, contrary to the illustration, the ion sheet is in reality not exactly aligned with the MCP pore rows. Some ions hit the MCP front surface, some enter into the MCP pores. The surface area represented by the pores relative to the total MCP area (the MCP aperture ratio) is an important, but fixed, factor in the MCP gain; it is on the order of 60% [5,15].

When an ion enters into an MCP pore and hits the wall there, it produces a number of secondary electrons. Most MCPs are constructed from lead glass with a typical composition [4] so that the secondary electron yield γ_k for an incident ion of type k depends mostly on the nature of the ion (for instance, its size) and on its energy [16]. The yield also depends on the ion incidence angle. Since the ion path deviates from the MCP normal by less than 3°, the variation of the yield with incidence angle is small. The secondary electrons are accelerated by the MCP gain potential, which is the electric potential difference between the MCP front and back surfaces (electrodes formed by vacuum deposition of inconel), and

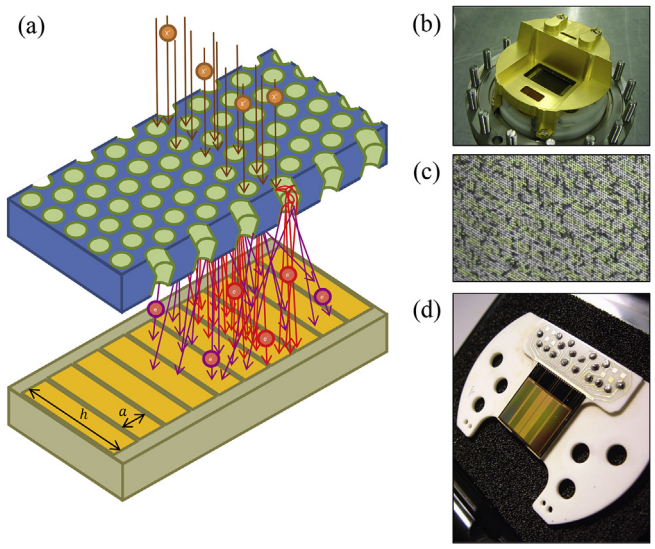

Fig. 1. DFMS detector assembly. (a) Ions with given mass-over-charge hit the MCP in a slab perpendicular to the mass analysis direction, yielding secondary electrons upon entering the MCP pores. Because of the potential difference between MCP front and back, these electrons gain energy and repeatedly collide with the pore walls (pore length-over-diameter ratio much larger than shown here). Upon exit the electrons are collected by adjacent anodes on the LEDA chip with width $a = 25\ \mu$m and height $h = 8$ mm (in red). Some of these electrons have enough energy to knock secondary electrons (in purple) off the LEDA, which are attracted back to the LEDA as an electric field is applied between MCP and LEDA [2]. The electrons produced by the ion beam thus create a mass peak several anodes wide. (b) The DFMS detector assembly houses the MCP-LEDA detector (central rectangular area), a Faraday cup (in front of the MCP-LEDA) and a channel electron multiplier (on the elevated section behind the MCP-LEDA). (c) A close-up view of the MCP with its hexagonally arranged 6 μm diameter pores. (d) LEDA chip on its ceramics substrate. Photographs courtesy of LATMOS and BIRA-IASB. (For interpretation of the references to color in this figure legend, the reader is referred to the Web version of this article.)

collide with the inner walls of the MCP pores multiple times, resulting in an electron cascade as illustrated in Fig. 1. The gain potential in DFMS can be set in 16 gain steps, each of which corresponds to an additional ~ 50 V and an accompanying amplification by a factor ~ 2.6 [2]. Note that the MCP behaves nonlinearly and may even saturate when the ion flux becomes too high. DFMS uses an automatic algorithm that sets the appropriate gain step, thereby avoiding the nonlinear or saturation regime as much as possible and limiting detector ageing [17]. The gain $G(p,t,g)$ depends on the gain step g as well as on time t and position p due to ageing. For the sake of convenience the overall gain is split in two factors, the overall gain and the position-dependent gain, so that

$$G(p,t,g) = G_{\mathrm{ov}}(g,t)G_{\mathrm{pgc}}(p,t,g) \tag{1}$$

with $\max_p G_{\mathrm{pgc}}(p,t,g) = 1$ as a normalization constraint. A typical overall gain curve can be found in Ref. [2]. When the MCP has been used, but not intensively, G_{pgc} shows a dip at the centre of the detector where most of the measured ion peaks are located and ageing is most pronounced, while $G_{\mathrm{pgc}} = 1$ near the edges [[18], supplementary material]. In that situation, G_{ov} depends only on g. After some time, however, also the edges degrade. Because of the normalization constraint the overall gain starts to decrease with time as well, on a time scale of months, at least 5 orders of magnitude longer than the time needed for measuring a spectrum. For the interpretation of a spectrum at a given time and a given gain step, therefore, the gain is $G(p) = G_{\mathrm{ov}}\ G_{\mathrm{pgc}}(p)$ and is assumed to be given.

In the present paper the position-dependent gain G_{pgc} is taken to be known. For the ROSINA DFMS mass spectrometer the original plan was to use the built-in gas calibration unit [14] to inject a constant flux of a neutral species in the instrument, and to scan the main ion peak over the detector by varying the commanded mass-over-charge (that is, changing all the potentials in the ion optics so that the ions arriving at the centre of the detector have the specified mass-over-charge value). As made clear in Fig. 2, both peak height and area are (almost) proportional to the value of G_{pgc} at the peak position. By measuring peak height or area as the peak moves over the detector, and by doing this for the different gain steps, $G_{\mathrm{pgc}}(p,g)$ can be obtained. Since the gas calibration unit failed before arrival at the comet, the cometary water peak was used instead; provisions were made to compensate for water abundance variations during the scan. Such position-dependent gain measurements were performed repeatedly throughout the mission, for various gain steps [[18], supplementary material] in order to assess detector ageing throughout the entire Rosetta mission.

The electrons that exit the MCP are registered by a linear CCD (Linear Electron Detector Array or LEDA) with two parallel rows of 512 charge collecting anodes and with independent read-out electronics for redundancy (channel A and B) [6]. The LEDA pixel size is $a = 25\ \mu$m in the mass analysis direction (pixel width) and

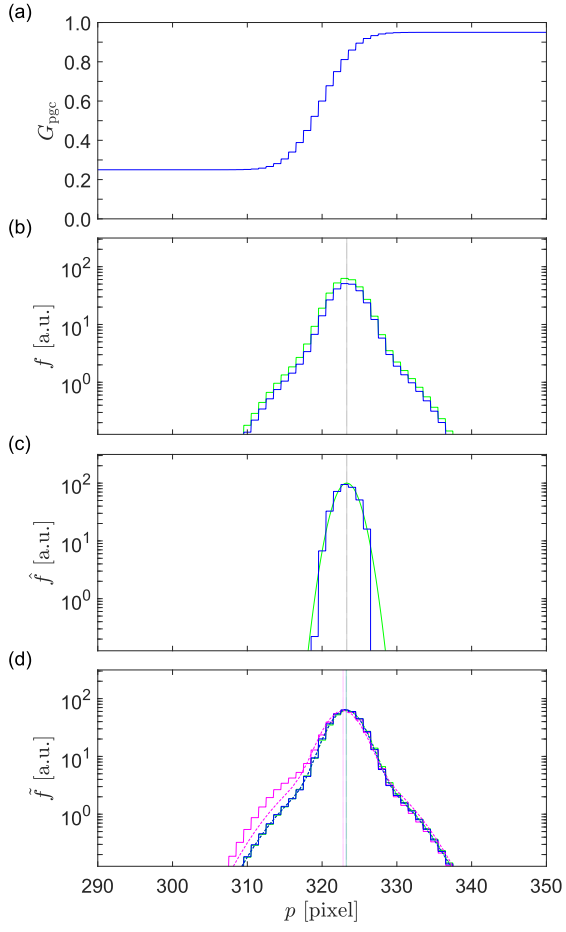

Figure 2. Simulated position-dependent gain correction for a single peak in HR mode. (a) Position-dependent gain correction factor in a limited pixel range near the detector centre. (b) Electron profile as it would be registered by the LEDA detector with (blue) and without (green) gain degradation. (c) Inferred incoming ion beam profile (blue) and actually imposed ion beam profile (green). (d) LEDA electron profile if there were no MCP degradation (green, hardly visible), after data restoration based on Eq. (15) (blue), and after classical data restoration using Eq. (17) (magenta); double Gaussian fits are also shown (dashed lines, corresponding colors).

$h = 8$ mm in the transverse direction (pixel height). The most energetic of the electrons exiting from the MCP (a few hundred eV) can produce secondary (and backscattered) electrons when hitting the LEDA anodes. An electric potential difference of 200 V is applied between MCP and LEDA to attract the escaping secondary electrons back to the LEDA [2]. The net effect is a redistribution on the LEDA of a fraction of the charges from the narrow incoming electron beam over a broader region (see Fig. 1). The strength of the applied electric potential between MCP and LEDA is a trade-off between the competing effects of, on the one hand, focusing the electrons exiting from the MCP and limiting the spread of the secondary electrons [2] and, on the other hand, increasing the electron energy and thereby enhancing the production of secondary electrons. The MCP-LEDA separation distance is as small as possible to reduce the spread of the MCP electrons as they cross the gap, while avoiding the risk of arcing due to the MCP-LEDA potential difference [2].

Consider an incident ion beam located at a position $\widehat{p}$ that is about as wide as the pore diameter ($\sim 6\ \mu$m). The electron intensity resulting from the electron cascades for all pores that receive ions, integrated perpendicular to the mass analysis direction, has a double Gaussian shape [2] where the primary Gaussian corresponds to the number of electrons produced by the MCP minus the ejected LEDA secondary electrons, and where the secondary Gaussian represents the redistributed LEDA secondary electrons. Let a Gaussian be given by

$$\phi(p, p^*, w) = e^{-\frac{(p-p^*)^2}{w^2}}, \tag{2}$$

where p is the position coordinate (related to the ion mass) and w is the half-width, with the normalization $\phi(p^*, p^*, w) = 1$. A double Gaussian shape centred on p^* is of the form

$$\psi(p, p^*, w_1, w_2, \alpha) = (1-\alpha)\phi(p, p^*, w_1) + \alpha\phi(p, p^*, w_2), \tag{3}$$

where w_1 and w_2 represent the half-widths of both Gaussians ($w_2 > w_1$) and where $0 \le \alpha < 1$ is the relative contribution of the second Gaussian. The electron distribution in the cascade then is $\psi^{(e)} = \psi(p, \widehat{p}, w_{e1}, w_{e2}, \alpha_e)/\sqrt{\pi}[(1-\alpha_e)w_{e1} + \alpha_e w_{e2}]$ when normalized such that $\int \psi^{(e)} \mathrm{d}p = 1$ and measured in the mass analysis direction.

The mass peaks are ion-optical images of the slit. The slit images ideally should be perpendicular to the mass analysis direction since the recorded mass peaks (which represent the signal integrated over the elongated anodes in the transverse direction) then have minimum width. Because of the symmetry of the construction, the maxima of corresponding mass peaks on anode channels A and B then are at the same position. In reality, the slit image is not exactly perpendicular to the mass analysis direction; it deviates by a slight misalignment angle $\theta \approx 0.1$–0.4°. As a consequence the maxima of corresponding peaks on both channels are a few pixels apart and the peaks are somewhat broader than in the ideal case. The transversely integrated electron distribution $\psi^{(e,\theta)}$ can be denoted as

$$\psi^{(e,\theta)}(p, \widehat{p}, w_{e\theta 1}, w_{e\theta 2}, \alpha_e) = \int_{-\delta/2}^{+\delta/2} \psi^{(e)}(p\cos\theta, (\widehat{p}+\xi)\cos\theta, w_{e1}, w_{e2}, \alpha_e)\, \mathrm{d}\xi \Big/ \Psi, \tag{4}$$

with $w_{e\theta 1,2} = w_{e1,2}/\cos\theta$ and $\delta = h\sin\theta$, and where Ψ is a normalization factor defined so that

$$\int_{-\infty}^{+\infty} \psi^{(e,\theta)}(p, \widehat{p}, w_{e\theta 1}, w_{e\theta 2}, \alpha_e)\, \mathrm{d}p = 1. \tag{5}$$

Because θ is so small, Eq. (4) can be simplified to

$$\psi^{(e,\theta)}(p, \widehat{p}, w_{e1}, w_{e2}, \alpha_e) = \int_{-\delta/2}^{+\delta/2} \psi^{(e)}(p, \widehat{p}+\xi, w_{e1}, w_{e2}, \alpha_e)\mathrm{d}\xi \Big/ \Psi. \tag{6}$$

For the aforementioned values of θ, the broadening δ amounts to 0.5–2.0 pixels.

The small LEDA pixel width implies a high mass resolution, while large pixel height ensures a large geometric factor. The anode charges are digitized by an analogue-to-digital converter (ADC) providing the counts per pixel. A DFMS mass spectrum is the sum of 3000 spectra of 6.554 ms each, for a total integration time $\Delta t = 19.66$ s; such accumulation avoids saturation of the anode capacitors and read-out counters and averages out thermal noise [19]. The resulting raw spectrum then must be calibrated to derive the ambient neutral gas densities [20].

3. Position-dependent gain correction

The interpretation of a raw mass spectrum must take into account the position-dependent gain correction. This section first addresses how the measured electron profile is produced in DFMS (forward model) before discussing how the incident ion profile can be derived from it (backward model). Finally, data restoration or "position-dependent gain correction" is considered so as to undo the effect of the position-dependent gain.

3.1. Electron profile measured by the LEDA

An incident ion beam feeds ions into a set of adjacent pores, each of which produces an electron cascade that has a certain spread. The net electron spectrum $\tilde{f}$, expressed as the measured number of electrons per pixel, therefore is a convolution of the ion beam profile $\widehat{f}$ and the electron cascade profile $\psi^{(e,\theta)}$ following

$$\tilde{f}(p) = \int_{p'} \widehat{f}(p')G(p')\psi^{(e,\theta)}(p, p')\mathrm{d}p', \tag{7}$$

which states that the electron intensity at position p is due to the contributions of electron cascades initiated by incident ions at nearby positions p'. The peaks in the resulting electron distribution can be represented by double Gaussians as well [21].

Integrating Eq. (7) over individual bins p_s with width Δp gives the number of electrons f collected in each of the n_p bins,

$$f(p_s) = \int_{p_s-\frac{\Delta p}{2}}^{p_s+\frac{\Delta p}{2}} \int_{p'} \widehat{f}(p')G(p')\psi^{(e,\theta)}(p, p')\mathrm{d}p'\mathrm{d}p. \tag{8}$$

In what follows, sub-pixels will be considered as bins, so that $\Delta p < 1$; hence the need to make a distinction between $\tilde{f}$ in electrons/pixel and f in electrons/bin. Equations (7) and (8) describe the MCP electron multiplication process as continuous in space, although it is discrete at the level of the pores. This approach is reasonable since the MCP pore diameter is smaller than the pixel width and also because the pores are not perfectly aligned in the transverse dimension.

DFMS mass peaks move over a certain pixel range with varying instrument temperature. Also, the ion beams arrive at the MCP front with a thickness spanning several pixels (as will be demonstrated later on). Therefore the gradients in $G_{\mathrm{pgc}}(p)$ due to ageing must be multiple pixels wide so that $G_{\mathrm{pgc}}(p)$ can be adequately represented by a discrete version at the pixel scale. Then Eq. (8) becomes

$$f(p_s) = G_{\mathrm{ov}} \sum_j G_{\mathrm{pgc}}\left(p_j\right) W\left(p_s, p_j\right) \tag{9}$$

with

$$W\left(p_s, p_j\right) = \int_{p_s-\frac{\Delta p}{2}}^{p_s+\frac{\Delta p}{2}} \int_{p_j-\frac{\Delta p}{2}}^{p_j+\frac{\Delta p}{2}} \widehat{f}(p')\psi^{(e,\theta)}(p,p')\mathrm{d}p'\mathrm{d}p. \tag{10}$$

While the sum runs over all pixels $j = 1,\ldots,n_p$, only the pixels in the neighbourhood of p_s actually contribute.

From an analysis of mass peak shapes, the shape of the electron cascade $\psi^{(e)}$ is reasonably well known [2]. Its half-width w_{e1} is 1.5–2 pixels and, as mentioned before, there is the 0.5–2 pixel broadening δ due to the misalignment. The ion beam half-width is a priori unknown and may vary somewhat, but it is typically a few pixels. Though $\psi^{(e,\theta)}$ and $\widehat{f}$ must be smooth and differentiable functions, they may vary significantly on the scale of a pixel. The computation of the integrals $W(p_s, p_j)$ can therefore be done in two ways. Either one uses the data at pixel resolution and one applies a higher order quadrature technique to integrate the smooth integrand, or one uses higher order interpolation to obtain the data at a finer spatial scale and then one performs the integration with a low order integrator. Both approaches are equivalent; the latter has been chosen here with a refinement factor $\zeta = 5$. Cubic interpolation is used to obtain all quantities on the scale of 1/5 th of the pixel width, in combination with the midpoint rule integrator. The above formalism then still holds, but the indices now run over $5n_p$ subpixels and Δp is correspondingly smaller. The integrals now are

$$W\left(p_s, p_j\right) \approx (\Delta p)^2 \widehat{f}\left(p_j\right) \psi^{(e,\theta)}\left(p_s, p_j\right). \tag{11}$$

Equations (9) and (11) represent a forward model describing how the electron output measured by the LEDA anodes can be computed from the incident ion beam profile.

3.2. Inferring the ion beam profile from the LEDA profile

The forward model states that the measured electron profile depends on the incident ion beam profile through

$$f_s = (\Delta p)^2 G_{\mathrm{ov}} \sum_j G_{\mathrm{pgcj}}\, \widehat{f}_j \psi_{sj}^{(e,\theta)} \tag{12}$$

where subscripts identify the (interpolated) pixel position where the quantities are evaluated. Solving the linear system

$$\begin{bmatrix} \ddots & & \\ & G_{\mathrm{pgcj}}\, \psi_{sj}^{(e,\theta)} & \\ & & \ddots \end{bmatrix} \begin{bmatrix} \vdots \\ \widehat{f}_j \\ \vdots \end{bmatrix} = \frac{1}{(\Delta p)^2 G_{\mathrm{ov}}} \begin{bmatrix} \vdots \\ f_s \\ \vdots \end{bmatrix} \tag{13}$$

recovers the ion beam profile $\widehat{f}$ from the measured LEDA electron profile f. Appendix A describes the solution procedure.

3.3. Data restoration

In the context of DFMS data processing the goal is not so much to obtain the ion beam shape, but rather to undo the effects of the position-dependent gain, i.e., to restore the data as if there had been no MCP gain degradation. Therefore, once $\widehat{f}$ has been computed, the forward model is applied with $G_{\mathrm{pgc}} \equiv 1$ to obtain the corrected electron output $\tilde{f}$. In a more compact matrix notation, one has

$$[\tilde{f}_s] = (\Delta p)^2 G_{\mathrm{ov}} \left[\psi_{sj}^{(e,\theta)}\right] \left[\widehat{f}_j\right]. \tag{14}$$

Combining Eqs. (13) and (14), $\widehat{f}_j$ is eliminated so that

$$[\tilde{f}_s] = \left[\psi_{sj}^{(e,\theta)}\right] \left[G_{\mathrm{pgcj}}\, \psi_{sj}^{(e,\theta)}\right]^{-1} [f_s]. \tag{15}$$

The suitability of this matrix equation for data restoration will be demonstrated in the following sections.

If the amount of detector ageing is limited, the variation of the position-dependent gain factor over a given mass peak (which typically covers some tens of pixels) cannot be very large. For the pixels around that peak, G_{pgcj} can be replaced by its average value there, or even by its local value G_{pgc}^* at the peak, without introducing significant error, so that

$$[\tilde{f}_s] = \frac{1}{G_{\mathrm{pgc}}^*} \left[\psi_{sj}^{(e,\theta)}\right] \left[\psi_{sj}^{(e,\theta)}\right]^{-1} [f_s], \tag{16}$$

that is,

$$\tilde{f}_s = \frac{f_s}{G_{\mathrm{pgc}}^*}. \tag{17}$$

This is the simpler form of data restoration that has been used in DFMS data analysis up to now [e.g. Refs. [20–24]]. One can regard this technique as being the result of the assumption that the electron cascade is less than 1 pixel wide, so that the number of electrons measured on a LEDA pixel only depends on the degradation of the MCP immediately above it. In the earlier phases of the Rosetta mission, the assumption of a slowly varying G_{pgc} is not too bad, especially in view of other and more important error sources, but in general this approach is suboptimal and it cannot explain the observed peak shapes and may sometimes even be misleading, as will be demonstrated below.

4. Validation using synthetic data

Fig. 2 illustrates the data restoration procedure on the basis of an artificially constructed example. It is assumed that there is only a single ion species present, whose mass-over-charge corresponds to pixel position 323.3. The ion beam impinges on the MCP with a Gaussian beam profile with $w_i = 2.0$ pixels. The MCP-LEDA combination is characterized by a double Gaussian electron cascade profile with $w_{e1} = 1.75$, $w_{e2} = 4.0 w_{e1}$, $\alpha_e = 0.05$, with a LEDA misalignment leading to $\delta = 2.0$. The MCP is assumed to have degraded considerably at the centre of the detector, where the position-dependent gain factor has dropped to 0.25, while it is 0.95 elsewhere (Fig. 2a). The resulting electron distribution that is expected at the LEDA in the case of a perfect MCP is shown in green in Fig. 2b, together with the distribution actually observed with the degraded MCP in blue. The example has been constructed in such a way that the ion beam coincides with the gradient in G_{pgc}. As a result, the recorded mass peak not only has a reduced height, but it is also slightly skewed, which causes a very minor shift of the centre of the observed peak; the position error is less than 1 pixel in the

present case. Overall the peak can still be represented fairly well by a double Gaussian. The ion beam profile is recovered by solving Eq. (13) (blue curve in Fig. 2c) and does not deviate much from the original Gaussian profile (green). The ion beam profile is necessarily narrower than the beam recorded by the LEDA because of the convolution with the electron cascade profile. Fig. 2d presents the LEDA profile for the case without MCP gain degradation (green, the same curve as in Fig. 2b, almost completely hidden below the blue line), with the classical restoration technique of Eq. (17) (magenta), and with the restoration based on the deconvolution of Eq. (15) (blue). The deconvolution technique reproduces the situation without MCP degradation almost exactly (relative error 4% on average), while classical restoration deviates significantly (relative error 85% on average). Because of the changing position-dependent gain, the peak loses its broadened double Gaussian shape and becomes asymmetric. This incorrectly seems to suggest that there would be a hidden contribution from a minor species with a lower mass. Fig. 2d shows double Gaussian fits to the three curves (dashed lines). A good double Gaussian fit is obtained for the deconvolution restoration (blue curve), although it is not perfect due to the broadening as a consequence of the misalignment ($\delta \neq 0$). The fit to the classical restoration (magenta) cannot deal with the skewing of the peak, being below it to the left and slightly above it to the right. The peak positions differ from the correct one by 0.5 pixels for classical restoration and by 0.1 pixels for the new technique.

In summary, the high resolution ion optics is so good that the slit image on the MCP is only a few pixels wide. As the gain is not too different for these few pixels, the LEDA will record essentially the convolution of the ion beam shape and the electron cascade, which is a somewhat broadened double Gaussian, multiplied with the position-dependent gain G^*_{pgc} at the peak position. The classical technique is manifestly inappropriate, since it corrects the electron counts recorded at each pixel by the value of G_{pgc} at that pixel, rather than using G^*_{pgc} at the peak position. The same is true for the low resolution mode. While the dispersion then is ~ 6.4 times smaller, the slit is 6.5 times larger, so that one ends up with a very similar situation.

A more complicated situation is considered in Fig. 3 where a second, less abundant, ion species is present at a slightly lower mass-over-charge, at pixel position 316.7. This second mass peak is superimposed on the first one, and gives rise to a shoulder on the left flank of the main mass peak (Fig. 3b). While the ion profile reconstruction shows two separated peaks (Fig. 3c), there is only a shoulder in the LEDA spectrum in view of the additional smoothing due to the nonzero width of the electron cascade. Fig. 3d demonstrates again that deconvolution works better than the classical technique. The figure also shows the two double Gaussians for each ion component and for both restoration techniques. The corrected profiles differ from the exact ones by only 5% on average for the deconvolution technique and 30% for the classical technique. Considering the contributions ascribed to each ion species, the double Gaussian fits for the primary peak yield an integrated area that deviates by 0.4% (deconvolution) and 1.6% (classical) from the correct one. For the secondary peak, the relative errors are larger, 1.5% (deconvolution) and 16% (classical). Such errors introduced during the data processing directly translate into an error on the incoming ion count rate, since the area under the peak is proportional to the ion count; they should be avoided whenever possible. These errors are, of course, strongly dependent on how the mass peaks are situated relative to the gradient in G_{pgc}. The above analysis has therefore been repeated for a changing position δp of the centre of the G_{pgc} gradient relative to the primary peak position (Fig. 4). Data restoration based on Eq. (15) always yields an error of less than 2% on the area under the peak. Classical restoration leads

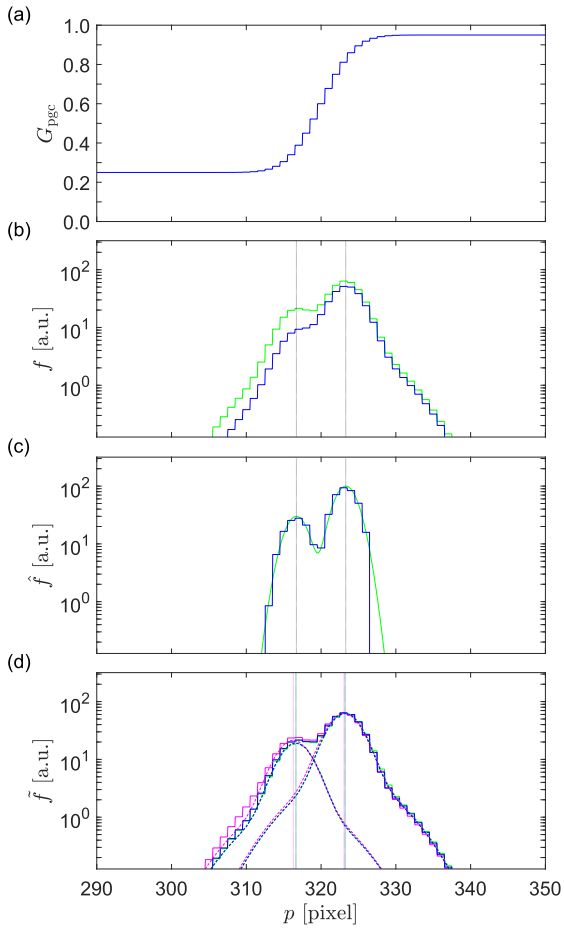

Fig. 3. Simulated position-dependent gain correction for a peak with a shoulder in HR mode. Same format as Fig. 2.

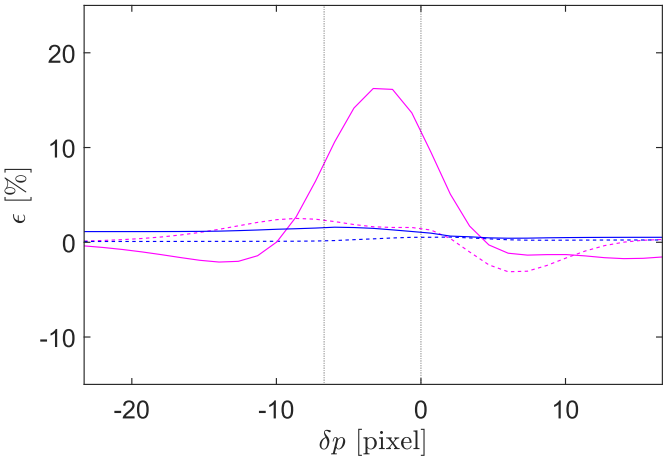

Fig. 4. Relative error ε on the mass peak area for the primary (dashed lines) and secondary (solid lines) species obtained with data restoration based on Eq. (15) (blue) and classical restoration using Eq. (17) (magenta) for spectra like that of Fig. 3, but for a range of relative positions δp between the centre of the G_{pgc} gradient and the primary peak position. (For interpretation of the references to color in this figure legend, the reader is referred to the Web version of this article.)

to an error of at most 4% for the primary peak, but of up to 15% for the secondary species. The errors decrease when moving away from the G_{pgc} gradient. Obviously, the incurred errors grow with

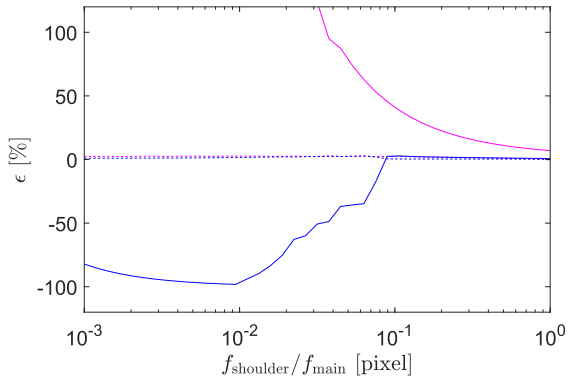

Fig. 5. Similar to Fig. 4 but for a range of relative intensities of both species.

the magnitude of the gradients. Great care therefore has to be taken with an MCP that has degraded, when the G_{pgc} values may vary significantly over a limited number of pixels. Much also depends on the size of the shoulder: If the contribution of the secondary peak in the example of Fig. 3 would have been 10 times less, then the relative error would have been even 10 times higher. This is illustrated in Fig. 5, which presents the errors for a range of intensities of the secondary peak relative to the primary peak. Classical restoration already leads to errors of > 10 % even if the shoulder is more than 1 /10 th of the primary peak. Deconvolution restoration is better, but it too fails when the shoulder becomes smaller. It should be noted, however, that the figure presents a worst-case situation, in which the peak-with-shoulder is located right at a major change in the position-dependent gain.

5. Validation using DFMS observations

In the previous section the merits of the proposed data restoration procedure have been illustrated using simulated MCP-LEDA spectra. This is not only an appropriate way to check the correctness of the approach, but it is especially useful as mass spectra acquired by DFMS at comet 67P usually show mass peaks that are the superposition of the contributions of several species. This is true for HR spectra, but even more so for LR spectra. In what follows, we focus on HR spectra, where the different species can be separated more easily.

Fig. 6 demonstrates the position-dependent gain correction techniques at a commanded mass-over-charge 29 amu /e. The mass spectrum was acquired on 1 October 2014 at 21:08:26 UTC, about 2 months into the comet phase of the Rosetta mission. Maximum gain (gain step 16) is needed since the species recorded at this mass are not very abundant. The spectra for channel A (left) and B (right) are very similar but not identical; the peaks for channel B are shifted by about $\Delta = 2$ pixels to the right compared with channel A. Note that $\Delta = (\delta_A + \delta_B)/2$. Since the peaks on channel A are always a bit narrower than on channel B, the estimate $\delta_A = 0.90\,\Delta/2$ and $\delta_B = 1.10\,\Delta/2$ has been made. For the electron cascade properties, the values $w_{e1} = 1.75$, $w_{e2} = 4.0 w_{e1}$, $\alpha_e = 0.05$ have been adopted; these must necessarily be valid for both channels. Indeed, the shape of the electron cascade only depends on the MCP and the potentials applied to it (which are uniform), the construction of the anode channels (which is identical for both), and the separation between MCP and LEDA (which is constant to the best of what was technically feasible). These values for the cascade properties are compatible with all that is known about the MCP-LEDA detector system, and they have been tested on a number of mass spectra. While these parameters are not very precisely known, the results of the restoration technique do not depend sensitively on their exact values (see Appendix).

Fig. 6a and d indicate that the position-dependent gain in the relevant region of the spectrum, at the centre of the MCP-LEDA detector, has degraded by a factor of almost 0.5 for channel A; the degradation is somewhat less for channel B. Serious degradation is thus already present early on in the comet phase of the Rosetta mission.

The spectra in Fig. 6b and e (raw data after offset removal, restored profile, and classically restored profile in green, blue, and magenta, respectively) highlight the presence of $^{13}C^{16}O^+$ and $H^{12}C^{16}O^+$ forming the broad left peak and of $^{12}C_2H_5^+$ forming the right peak. $^{12}CH_3^{14}N^+$ is a minor contribution to the right peak in the form of a shoulder. The deconvolution and classically restored spectra look similar, but they do show non-negligible differences. In the region of deep degradation (channel A, pixels 260–265) the classical restoration overestimates the actual values since it is based on the local minimum in G_{pgc} of around 0.52, while the actual position-dependent gain that should apply there is closer to that of the $^{13}C^{16}O^+$ peak (0.73). As already discussed in the previous section, this deforms the peak shape. There are also some small differences near the $^{12}CH_3^{14}N^+$ peak. The conclusion is that both techniques agree well for primary peaks, but important differences can arise at secondary peaks and shoulders.

Fig. 6c and f shows the reconstructed ion profiles (in blue), while the green line is the ion profile obtained by using the same w_{e1} and w_{e2}, but doubling the value of α_e. This gives more weight to the flanks of the peaks and effectively suppresses noise in the solution; it makes the peaks stand out more clearly. Shaded green zones indicate where both reconstructed ion profiles rise above the noise and do not differ by more than a factor of 2. Note that the ion profiles present an isolated maximum for $^{12}CH_3^{14}N^+$ rather than a shoulder as in the electron profile. It should also be remarked that the recovered ion beam shape is basically that of a single Gaussian, something that has been verified by experiments with the DFMS copy in the laboratory.

A similar situation is seen in Fig. 7 for the mass spectrum at mass-over-charge 28 amu /e that was acquired on 1 October 2014 at 21:07:50 UTC at a gain step 13, immediately preceding the spectrum of Fig. 6. Note that the position-dependent gain profile is different since this spectrum is taken at another gain setting; the depletion for channel A goes down to a factor 0.3. The spectra show clear peaks or shoulders for $^{12}C^{16}O^+$, $^{14}N_2^+$, $^{12}CH_2^{14}N^+$, and $^{12}C_2H_4^+$. The $C^{16}O^+$ ions are responsible for the main peak; they come from the ionization and fragmentation of CO_2 and of CO, the 2nd and 3rd most abundant neutral species in the comet atmosphere [20]. A typical feature is the pronounced shoulder that marks the discovery of N_2 [see also [25], Fig. 1]. The reconstructed ion profile identifies the various species even more clearly. There are again some differences between the deconvolution and the classical restoration results. Since the $^{12}C^{16}O^+$ maximum is situated almost at the place of deepest degradation, the classical restoration underestimates the contribution (magenta line below the blue line for channel A, pixels 270–280). This has an immediate effect on the estimated importance of the N_2 contribution. The conclusion is thus always the same: Both restoration techniques work well for the major peaks, but the effect of not using the correct restoration procedure is strongest for secondary contributions.

6. Conclusion

MCP ageing in the Rosetta ROSINA DFMS MCP-LEDA detector causes the total gain to decrease. Ageing of the MCP consists of two components. First, there is a reduction of the secondary electron yield of an impacting ion on the inner walls of the MCP pores, close

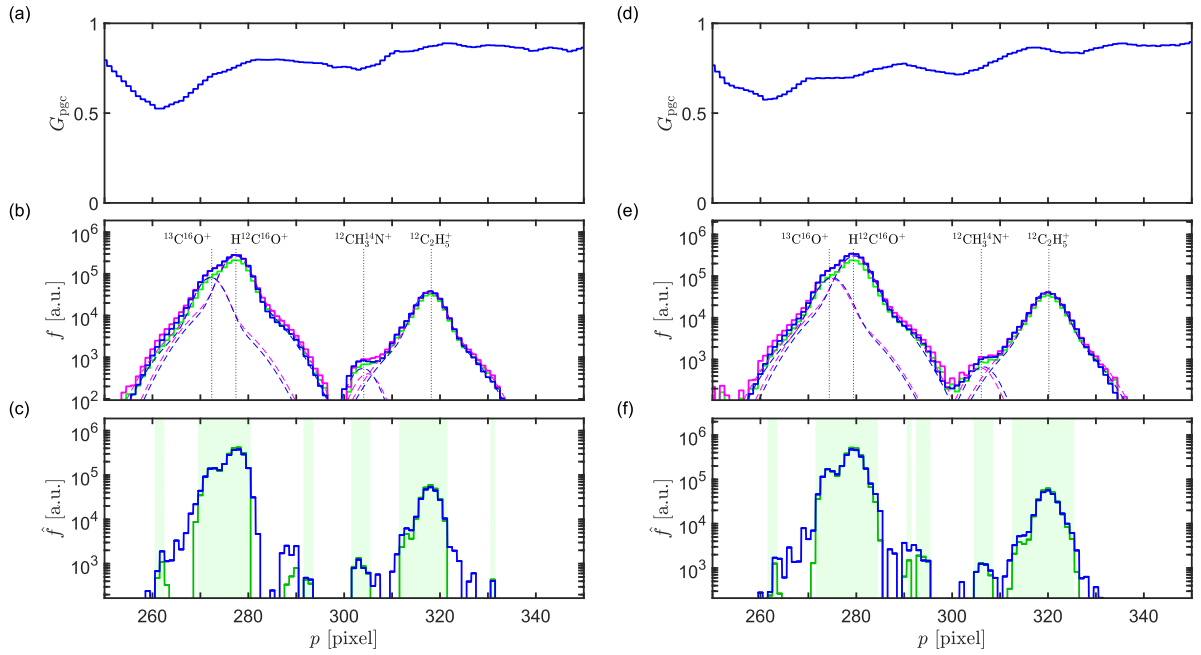

Fig. 6. Position-dependent gain correction for DFMS spectrum around 29 amu /e on 1 October 2014 at 21:08:26 UTC (gain step 16): (a) G_{pgc} for channel A; (b) raw LEDA counts (green), restored profile (blue), classical restoration (magenta), with dashed lines showing the contributions of the individual species; (c) reconstructed ion profile without (blue) and with noise suppression (green, see text) and peak regions (shaded green); (d–f) same format for channel B. (For interpretation of the references to color in this figure legend, the reader is referred to the Web version of this article.)

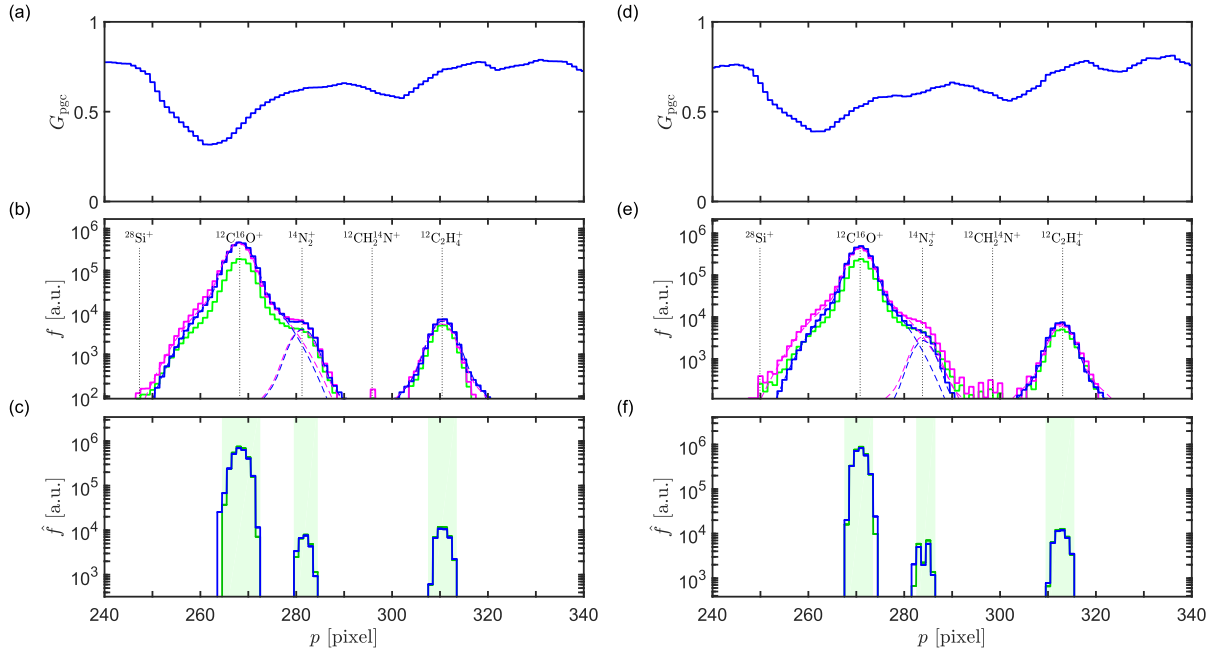

Fig. 7. Position-dependent gain correction for DFMS spectrum around 28 amu /e 1 October 2014 at 21:07:50 UTC (gain step 13). Same format as in Fig. 6.

to the MCP front surface. Second, farther down the pores and especially close to the MCP back surface there may be a reduction of the efficiency with which impacting electrons create secondary electrons. Because one cannot immediately separate both effects, ageing is usually modelled by the introduction of a position-dependent reduction of the gain, while the secondary electron yields of impacting ions are kept constant. Because of the aforementioned effects, the position-dependent gain is a function of the gain potential.

MCP ageing is uneven, leading to gradients in the position-dependent gain. This paper has introduced a data restoration technique to undo the effects of the position-dependent gain by means of a deconvolution, based on a reasonable estimate of the shape of the electron cascade that exits from the MCP pores and of the LEDA secondary electron redistribution. It has been shown that this technique is better than the classical technique that essentially

assumes that the electron cascade is <1 pixel wide, which is equivalent to assuming that the position-dependent changes are weak.

The classical data restoration technique may lead to asymmetric peaks for an individual ion beam, while the DFMS peaks are surprisingly symmetric. The deconvolution technique resolves this problem.

As has been demonstrated, the classical technique often works well, with errors of a few percent, but occasionally higher. Other uncertainties in the data interpretation pipeline, such as the Poisson counting statistics error, uncertainties on the position-dependent gain itself, uncertainties on the sensitivities, etc., can be significantly larger so that the use of the classical technique appears to be justified.

However, determining the contribution of a less abundant species superposed on the mass peak of a highly abundant species is very sensitive. It has been demonstrated that the relative error on the abundance of the secondary species can be high, especially if the secondary contribution is small and causes a small shoulder on the flank of the primary peak. In such cases it is strongly preferable to use the data restoration technique introduced here. This issue with shoulders superposed on other peaks occurs quite often in practice, and it is aggravated in particular when the signal-to-noise ratio in the spectra is low [e.g. Refs. [24,26]].

One potentially dangerous consequence of using classical restoration in the case of shoulders is that the error depends in a systematic manner on the relative contributions of the primary and secondary species, i.e., there would be a modification of the correlation between the estimated abundances of the primary and secondary species. This problem is exacerbated in the situation where the position of the peak with the shoulder relative to the G_{pgc} gradient changes with time. This happens when the instrument temperature (magnet temperature in particular) varies. Classical restoration then introduces a systematic temperature-dependent modulation on the estimated abundance of the secondary species.

While the present paper has focused on the DFMS neutral mode, the deconvolution technique can equally well be applied to the ion mode. In the ion mode, the ambient ions are streaming into the instrument and are subject to the same acceleration potential as a function of commanded mass-over-charge as in the neutral mode, and to the same electrostatic and magnetic sectors. The only difference lies in the deactivation of the ion repeller grid at the instrument entrance and of the electron ionization source. The ion distribution arriving at the MCP might therefore still retain a signature of the incident ion energy distribution, though modulated by spacecraft potential and other effects [27]. If that energy distribution is broad enough, the reconstructed ion spectrum would somehow reflect this energy distribution. Ions of cometary origin, however, are rather cold and so this would be of only limited value for DFMS.

Disclosure

The authors report no conflicts of interest in this work.

Acknowledgements and funding

The authors thank the following institutions and agencies: Part of the work at BIRA-IASB was supported by the Belgian Science Policy Office via PRODEX/ROSINA PEA 90020 and an Additional Researchers Grant (Ministerial Decree of 2014-12-19). AG thanks FNRS for a FRIA research grant. Work at UoB was funded by the State of Bern, the Swiss National Science Foundation (200021_165869 and 200020_182418), and by the European Space Agency PRODEX Program. Work at Southwest Research institute was supported by subcontract no. 1496541 from the Jet Propulsion Laboratory. Work at LATMOS has been carried out thanks to the support of the A*MIDEX project (nr. ANR-11-IDEX-0001-02) funded by the "Investissements d'Avenir" French Government program, managed by the French National Research Agency (ANR), and of CNES grants. Work at the University of Michigan was funded by NASA under contract JPL-1266313. The results from ROSINA would not be possible without the efforts of the many engineers, technicians, and scientists involved in the mission and in the ROSINA instrument team over the past 20 years, whose contributions are gratefully acknowledged. Rosetta is an ESA mission with contributions from its member states and NASA. All ROSINA data are available from the PSA archive of ESA and the PDS archive of NASA. Data and software used to produce the tables and figures in this manuscript are available from the authors upon request.

Appendix A. Iterative solver for data restoration

This Appendix describes a solution technique for Eq. (13). With $\beta = 1/G_{\mathrm{ov}}$, that system can be written as

$$\Delta p\, \mathbf{G}\, \mathbf{\Psi}\, \widehat{\mathbf{f}} = \beta\, \tilde{\mathbf{f}}, \tag{A.1}$$

where $\mathbf{G} = \mathrm{diag}\, G_{\mathrm{pgc}}$ has the position-dependent gains on its diagonal and $\mathbf{\Psi}$ is symmetric with positive elements $\psi_{ij}^{(e,\theta)}$.

The problem is ill-posed. This is addressed by adding a smoothness constraint and considering the least-squares target function

$$F = \sum_{i=1}^{n_p} \left(\Delta p \sum_{j=1}^{n_p} G_{\mathrm{pgc}j}\, \psi_{ij}^{(e,\theta)} \widehat{f}_j - \beta \tilde{f}_i \right)^2 + \sum_{i=2}^{n_p-1} \left(\frac{\widehat{f}_{i-1} - 2\widehat{f}_i + \widehat{f}_{i+1}}{(\Delta p)^2} \right)^2 = \left\| \Delta p \mathbf{G} \mathbf{\Psi} \widehat{\mathbf{f}} - \beta \tilde{\mathbf{f}} \right\|^2 + \gamma \left\| \mathbf{C} \widehat{\mathbf{f}} \right\|^2. \tag{A.2}$$

The parameter γ is a dimensionless and normalized weight factor. The first term in Eq. (A.2) captures the system residuals, while the second term represents the second derivatives of $\widehat{f}$ and thus its smoothness. For $\gamma > 1$, more emphasis is given to the smoothness constraint, for $\gamma < 1$ less. A value $\gamma = 10^{-4}$ has been chosen here, giving a sufficiently large regularization term while keeping the imposed smoothness to a minimum. Note that the formulation is such that the value of γ is independent of the choice of n_p with which the spectrum is discretized. The minimum of F is found from $\partial F / \partial \widehat{f}_k = 0$, which leads to

$$\sum_{j=1}^{n_p} \left[\left(G_{\mathrm{pgc}j}\, G_{\mathrm{pgc}k}\, (\Delta p)^2 \sum_{i=1}^{n_p} \psi_{ij}^{(e,\theta)} \psi_{ik}^{(e,\theta)} \right) + \sum_{i=1}^{n_p} \gamma\, c_{ij}\, c_{ik} \right] \widehat{f}_j = \beta\, G_{\mathrm{pgc}k} \sum_{i=1}^{n_p} \psi_{ik}^{(e,\theta)} f_i \tag{A.3}$$

for each $k = 1, \ldots, n_p$, or

$$\mathbf{A} \widehat{\mathbf{f}} = \mathbf{b}. \tag{A.4}$$

This symmetrized linear $n_p \times n_p$ system is a well-posed one.

A simple and robust way to solve system A.3 is by using a direct method. Because of the smoothing term, the numerical condition is reasonable but the solution may contain negative values, which must be filtered out. In practice, the system is solved for various values of γ to identify and remove noise from the solution.

The solution process can be substantially accelerated by noting

that the system of Eq. (A.4) decouples into separate subsystems wherever **b** is zero, since $\widehat{\mathbf{f}}$ has to vanish there too; dropping all rows and columns corresponding to these unknowns reduces the size of the system substantially.

It should be noted that, while Eq. (13) represents an ill-posed problem, Eq. (15) is well-posed: Even if the ion beam profile $\widehat{f}$ may not be computed precisely, $\tilde{f}$ is well-defined. This explains why the introduction of the smoothness term and the precise value of γ actually do not matter much.

Appendix B. Supplementary material

A set of MatLab routines for performing position-dependent gain correction is publicly available from Ref. [28].

Appendix C. Supplementary data

Supplementary data to this article can be found online at https://doi.org/10.1016/j.ijms.2019.116232.

References

[1] E. de Hoffmann, V. Stroobant, Mass Spectrometry - Principles and Applications, third ed., John Wiley & sons, 2007.

[2] J.-J. Berthelier, J.-M. Illiano, D. Nevejans, E. Neefs, E. Arijs, N. Schoon, High resolution focal plane detector for a space-borne magnetic mass spectrometer, Int. J. Mass Spectrom. 215 (1–3) (2002) 89–100, https://doi.org/10.1016/S1387-3806(02)00527-4.

[3] S. Medhe, Mass spectrometry: detectors review, Chem. Biomol. Eng. 3 (4) (2018) 51–58, https://doi.org/10.11648/j.cbe.20180304.11.

[4] J.L. Wiza, Microchannel plate detectors, Nucl. Instrum. Methods 162 (1979) 587–601, https://doi.org/10.1016/0029-554X(79)90734-1.

[5] T. Gys, Micro-channel plates and vacuum detectors, Nucl. Instrum. Methods Phys. Res. A 787 (2015) 254–260, https://doi.org/10.1016/j.nima.2014.12.044.

[6] D. Nevejans, E. Neefs, S. Kavadias, P. Merken, C. Van Hoof, The LEDA512 integrated circuit anode array for the analog recording of mass spectra, Int. J. Mass Spectrom. 215 (1) (2002) 77–87, https://doi.org/10.1016/S1387-3806(01)00549-8.

[7] C.L. Joseph, R. Bybee, V. Argabright, Stability coefficients for the multianode microchannel array detector, Rev. Sci. Instrum. 69 (1998) 1898–1905, https://doi.org/10.1063/1.1148861.

[8] F.F. Umarov, A.A. Dzhurakhalov, Ion bombardment-induced surface effects in materials, IntechOpen (2016) 359–391, https://doi.org/10.5772/62731. Ch. 14.

[9] P.M.L. Hedberg, P. Peres, F. F, L. Renaud, Multiple ion counting measurement strategies by SIMS – a case study from nuclear safeguards and forensics, J. Anal. At. Spectrom. 30 (2015) 2516–2524, https://doi.org/10.1039/c5ja00382b.

[10] D.O. Khataria, Microchannel plates at high rates: the challenges for future space plasma missions, J. Vac. Sci. Technol. B 24 (2) (2006) 1040–1044, https://doi.org/10.1116/1.2183786.

[11] M. Müller, T. Mikoviny, A. Wisthaler, Detector aging induced mass discrimination and non-linearity effects in PTR-ToF-MS, Int. J. Mass Spectrom. (2014) 365–366, https://doi.org/10.1016/j.ijms.2013.12.008, 93–97.

[12] E.H. Eberhardt, Gain model for microchannel plates, Appl. Opt. 18 (9) (1979) 1418–1423, https://doi.org/10.1364/AO.18.001418.

[13] R.A. Baragiola, Current topics in kinetic electron emission from solids, in: A. Gras-Marti, H.M. Urbassek, N.R. Arista, F. Flores (Eds.), Interaction of Charged Particles with Solids and Surfaces, vol. 271, Springer, Boston, MA, 1991, pp. 443–458, https://doi.org/10.1007/978-1-4684-8026-9_19, of Nato ASI Series (Series B: Physics).

[14] H. Balsiger, K. Altwegg, P. Bochsler, P. Eberhardt, J. Fischer, S. Graf, A. Jäckel, E. Kopp, U. Langer, M. Mildner, J. Müller, T. Riesen, M. Rubin, S. Scherer, P. Wurz, S. Wüthrich, E. Arijs, S. Delanoye, J. De Keyser, E. Neefs, D. Nevejans, H. Rème, C. Aoustin, C. Mazelle, J.-L. Médale, J.A. Sauvaud, J.-J. Berthelier, J.-L. Bertaux, L. Duvet, J.-M. Illiano, S.A. Fuselier, A.G. Ghielmetti, T. Magoncelli, E.G. Shelley, A. Korth, K. Heerlein, H. Lauche, S. Livi, A. Loose, U. Mall, B. Wilken, F. Gliem, B. Fiethe, T.I. Gombosi, B. Block, G.R. Carignan, L.A. Fisk, J.H. Waite, D.T. Young, H. Wollnik, Rosina - Rosetta orbiter spectrometer for ion and neutral analysis, Space Sci. Rev. 128 (1–4) (2007) 745–801, https://doi.org/10.1007/s11214-006-8335-3.

[15] B. Brehm, J. Grosser, T. Ruscheinski, M. Zimmer, Absolute detection efficiencies of a microchannel plate detector for ions, Meas. Sci. Technol. 6 (1995) 953–958, https://doi.org/10.1088/0957-0233/6/7/015.

[16] R. Meier, P. Eberhardt, Velocity and ion species dependence of the gain of microchannel plates, Int. J. Mass Spectrom. Ion Process. 123 (1993) 19–27, https://doi.org/10.1016/0168-1176(93)87050-3.

[17] P. Eberhardt, K. Altwegg, DFMS Instrument Modes and Measurement Sequences, Appendix D1 to the ROSINA User Manual, Tech. Rep. RO-ROS-MAN-1010, Universität Bern, 2002.

[18] I. Schroeder, K. Altwegg, H. Balsiger, J.-J. Berthelier, J. De Keyser, B. Fiethe, S.A. Fuselier, S. Gasc, T.I. Gombosi, M. Rubin, T. Sémon, C.-Y. Tzou, S.F. Wampfler, P. Wurz, $^{16}O/^{18}O$ ratio in water in the coma of comet 67P/Churyumov-Gerasimenko measured with the Rosetta/ROSINA double-focusing mass spectrometer, A&A 33806 (2018) 1–12, https://doi.org/10.1051/0004-6361/201833806.

[19] E. Neefs, J.-M. Illiano, D. Nevejans, DFMS MCP-LEDA Detector Calibration in CASYMS – Flight Spare Model, Tech. Rep. ROS-BIRA-RP-15, Belgian Institute for Space Aeronomy, 2002.

[20] L. Le Roy, K. Altwegg, H. Balsiger, J.-J. Berthelier, A. Bieler, C. Briois, U. Calmonte, M.R. Combi, J. De Keyser, F. Dhooghe, B. Fiethe, S.A. Fuselier, S. Gasc, T.I. Gombosi, M. Hässig, A. Jäckel, M. Rubin, C.-Y. Tzou, Inventory of the volatiles on comet 67P/Churyumov-Gerasimenko from Rosetta/ROSINA, A&A 583 (26450) (2015) A1, https://doi.org/10.1051/0004-6361/201526450.

[21] J. De Keyser, F. Dhooghe, A. Gibbons, K. Altwegg, H. Balsiger, J.-J. Berthelier, C. Briois, U. Calmonte, G. Cessateur, E. Equeter, B. Fiethe, S.A. Fuselier, T.I. Gombosi, H. Gunell, M. Hässig, L. Le Roy, R. Maggiolo, E. Neefs, M. Rubin, T. Sémon, Correcting peak deformation in Rosetta's ROSINA/DFMS mass spectrometer, Int. J. Mass Spectrom. 393 (2015) 41–51, https://doi.org/10.1016/j.ijms.2015.10.010.

[22] A. Bieler, K. Altwegg, H. Balsiger, A. Bar-Nun, J.-J. Berthelier, P. Bochsler, C. Briois, U. Calmonte, M. Combi, J. De Keyser, E.F. van Dishoeck, B. Fiethe, S.A. Fuselier, S. Gasc, T.I. Gombosi, K.C. Hansen, M. Hässig, A. Jäckel, E. Kopp, A. Korth, L. Le Roy, U. Mall, R. Maggiolo, B. Marty, O. Mousis, T. Owen, H. Rème, M. Rubin, T. Sémon, C.-Y. Tzou, J.H. Waite, C. Walsh, P. Wurz, Abundant molecular oxygen in the coma of comet 67P/Churyumov-Gerasimenko, Nature 526 (2015) 678–681, https://doi.org/10.1038/nature15707.

[23] U. Calmonte, K. Altwegg, H. Balsiger, J.J. Berthelier, A. Bieler, G. Cessateur, F. Dhooghe, E.F. van Dishoeck, B. Fiethe, S.A. Fuselier, S. Gasc, T.I. Gombosi, M. Hässig, L. Le Roy, M. Rubin, T. Sémon, C.-Y. Tzou, S.F. Wampfler, Sulphur-bearing species in the coma of comet 67P/Churyumov-Gerasimenko, MNRAS 462 (2016) S253–S273, https://doi.org/10.1093/mnras/stw2601.

[24] F. Dhooghe, J. De Keyser, K. Altwegg, C. Briois, H. Balsiger, J.-J. Berthelier, U. Calmonte, G. Cessateur, M.R. Combi, E. Equeter, B. Fiethe, N. Fray, S. Fuselier, S. Gasc, A. Gibbons, T. Gombosi, H. Gunell, M. Hässig, M. Hilchenbach, L. Le Roy, R. Maggiolo, U. Mall, B. Marty, E. Neefs, H. Rème, M. Rubin, T. Sémon, C.-Y. Tzou, P. Wurz, Halogens as tracers of protosolar nebula material in comet 67P/Churyumov-Gerasimenko, MNRAS 472 (2017) 13361345, https://doi.org/10.1093/mnras/stx1911.

[25] M. Rubin, K. Altwegg, H. Balsiger, A. Bar-Nun, J.-J. Berthelier, A. Bieler, P. Bochsler, C. Briois, U. Calmonte, M. Combi, J. De Keyser, F. Dhooghe, P. Eberhardt, B. Fiethe, S.A. Fuselier, S. Gasc, T.I. Gombosi, K.C. Hansen, M. Hässig, A. Jäckel, E. Kopp, A. Korth, L. Le Roy, U. Mall, B. Marty, O. Mousis, T. Owen, H. Rème, T. Sémon, C.-Y. Tzou, H. Waite, P. Wurz, Molecular nitrogen in comet 67P/Churyumov-Gerasimenko indicates a low formation temperature, Science 348 (6231) (2015) 232–235, https://doi.org/10.1126/science.aaa6100.

[26] K. Altwegg, H. Balsiger, J.J. Berthelier, A. Bieler, U. Calmonte, J. De Keyser, B. Fiethe, S.A. Fuselier, S. Gasc, T.I. Gombosi, T. Owen, L. Le Roy, M. Rubin, T. Sémon, C.-Y. Tzou, D2O and HDS in the coma of 67P/Churyumov–Gerasimenko, Phil. Trans. R. Soc. A 375 (2017) 20160253, https://doi.org/10.1098/rsta.2016.0253.

[27] S.A. Fuselier, K. Altwegg, H. Balsiger, J.J. Berthelier, A. Bieler, C. Briois, T.W. Broiles, J.L. Burch, U. Calmonte, G. Cessateur, M. Combi, J. De Keyser, B. Fiethe, M. Galand, S. Gasc, T.I. Gombosi, H. Gunell, K.C. Hansen, M. Hässig, A. Jäckel, A. Korth, L. Le Roy, U. Mall, K.E. Mandt, S.M. Petrinec, S. Raghuram, H. Rème, M. Rinaldi, M. Rubin, T. Sémon, K.J. Trattner, C.-Y. Tzou, E. Vigren, J.H. Waite, P. Wurz, ROSINA/DFMS and IES observations of 67P: ion-neutral chemistry in the coma of a weakly outgassing comet, A&A 583 (2015) A2, https://doi.org/10.1051/0004-6361/201526210.

[28] J. De Keyser, Position-dependent Microchannel Plate Gain Correction in Rosetta's ROSINA/DFMS Mass Spectrometer: Supplementary Materials, 2019, https://doi.org/10.18758/71021046.